The DOI for this manuscript is doi: 10.1175/JAMC-D-17-0068.1

The final published version of this manuscript will replace the preliminary version at the above DOI once it is available.

If you would like to cite this EOR in a separate work, please use the following full citation:

Kennedy, P., M. Thurai, C. Praz, V. Bringi, A. Berne, and B. Notaroš, 2018: Variations in Snow Crystal Riming and ZDR: A Case Analysis. J. Appl. Meteor. Climatol. doi:10.1175/JAMC-D-17-0068.1, in press.

Variations in Snow Crystal Riming and Z_{DR}: A Case Analysis

Patrick Kennedy[(1)], Merhala Thurai[(2)], Christophe Praz[(3)], V. N. Bringi[(2)], Alexis Berne[(3)], and Branislav M. Notaroš[(2)†]

[(1)]CSU-CHILL National Weather Radar Facility, Colorado State University, Greeley, CO, USA

[(2)]Department of Electrical and Computer Engineering, Colorado State University, Fort Collins, CO, USA

[(3)]Environmental Remote Sensing Laboratory, École Polytechnique Fédérale de Lausanne, Lausanne, Switzerland

Submitted to **Journal of Applied Meteorology and Climatology**, 12 March 2017

Revised: 1 August 2017

Revision 2: 21 October 2017

Revision 3: 12 December 2017

[†]Corresponding Author:
Branislav M. Notaroš
Colorado State University
Department of Electrical and Computer Engineering
1373 Campus Delivery
Fort Collins, CO 80523, USA
Phone: (970) 491-3537, Fax: (970) 491-2249
Web: www.engr.colostate.edu/~notaros
E-mail: notaros@colostate.edu

Abstract

A case study in terms of variations in differential reflectivity (Z_{DR}) observed at X-band and snow crystal riming is presented for a light snow event that occurred near Greeley, Colorado on 26–27 November 2015. In the early portion of the event, Z_{DR} values at near surface levels were low (~0 to 0.25 dB). During a second time period approximately eight hours later, Z_{DR} values became distinctly positive (~ +2 to +3 dB). Digital photographs of the snow particles were obtained by a Multi-Angle Snowflake Camera (MASC) installed at a range of 13 km from the radar. Image processing and machine learning techniques applied to the MASC data showed that the snow particles were more heavily rimed during the low Z_{DR} time period. The aerodynamic effects of these rime deposits promoted a wider distribution of hydrometeor canting angles. The shift toward more random particle orientations underlies the observed reduction in Z_{DR} during the period where more heavily rimed particles were observed in the MASC data.

1. Introduction

Synoptic scale mid-latitude precipitation systems often have vertical extents that include much of the troposphere. This depth spans a wide temperature range; the organized upward air motions in these systems also promote significant supercooled liquid water concentrations. These conditions support several hydrometeor development processes including active dendritic growth near the −15°C level (Kennedy and Rutledge 2011), and areas of local riming enhancement and secondary ice production (Giangrande et al. 2016). These cloud microphysical complexities, and especially the variability in the microwave backscattering properties of different ice particle types as they undergo riming, contribute to the challenge of detecting riming conditions using conventionally scanning dual-polarization radars (Vogel et al. 2015).

Historically, differential reflectivity (Z_{DR}) has been shown to provide useful information on the drop size distributions as well as shape and orientation characteristics of raindrops (Seliga and Bringi 1976; Bringi et al. 1998). The interpretation of the Z_{DR} observed from snow is more complicated. Unlike liquid drops, frozen hydrometeors do not have well-defined size – shape relationships. Nevertheless, a large number of polarimetric radar measurements show fascinating signatures especially related to positive Z_{DR} and K_{DP} aloft (e.g., Matrosov et al. 2001; Kennedy and Rutledge 2011; Kumjian et al. 2013; Ryzhkov et al. 2016; Williams et al. 2015). Frozen precipitation particles generally exhibit larger spatial orientation angle fluctuations than rain drops (Ryzhkov et al. 2011; Matrosov et al. 2005), and furthermore the scattering properties of ice crystals can be dependent on the intricate, detailed particle structures (e.g., Botta et al. 2011; Kuo et al. 2016; Lu et al. 2016). The refractive index properties of snowflakes also vary according to the amount of air contained in the overall ice structure (Smith 1984). When riming deposits frozen cloud droplets on the outer surface of snow particles, snowflake shape, fall orientation, and density characteristics are all altered, which in turn complicates the interpretation of polarimetric radar data. It follows that in-situ measurements of these particle characteristics are important but difficult to obtain at the required resolution. Aircraft-based imaging probes yield important information on particle size and shape (crystal habit), as well as qualitative indication of riming and environmental conditions favorable for crystal formation, but the imaging is generally in one plane only and as a result complete orientation information is typically not available (Wolde and Vali 2001). Under horizontally homogeneous conditions, the elevation angle dependence of polarimetric radar data can reveal information of ice crystal orientation or "flutter" (Matrosov et al. 2005).

This study is motivated by the physical reasons underpinning observed differential reflectivity (Z_{DR}) variations on the order of 2 dB that occurred near the ground by a 9 GHz (X-band) radar during a multi-hour, widespread, light snow event in the high plains of Colorado. During this event, digital photographs of the snow particles were obtained by a Multi-Angle Snowflake Camera (MASC; Garrett et al. 2012) that was located at a range of 13 km from the radar. Image processing techniques that automatically extract a variety of solid hydrometeor characteristics from MASC data sets have recently been developed (Praz et al. 2017). In addition to the classification of particles by habit, these image processing procedures also provide information on the axis ratios, orientation angles, and riming level of the imaged particles. Garrett et al. (2015) use a simpler approach to determine the statistics of aspect ratio and orientation angle of snow, rimed snow, and graupel based on MASC data. Using herein the Praz et al. (2017) methodology, MASC-based snow particle characteristics are examined from two time periods that displayed appreciably different Z_{DR} regimes. During the low Z_{DR} time period, the MASC image analyses showed that consistently higher levels of riming existed. These rimed particles, especially at larger diameters, also had a broader distribution of orientation angles and slightly larger (more spherical) axis ratios. These snow particle orientation characteristics are consistent with the observed lower Z_{DR} levels. During the contrasting 2 to 3 dB Z_{DR} time period, riming was less evident in the MASC images and the particles maintained more horizontal orientation angles.

This paper is organized as follows. Section 2 describes the instrumentation site and briefly the Multi-Angle Snowflake Camera system and the CSU-CHILL radar's X-band system which is used herein, as well as the larger scale meteorology of the event which occurred on 26-27 November 2015. Section 3 describes in detail the radar and MASC data for the two periods characterized by different Z_{DR} signatures, as well as microphysical characteristics which form the central core of this study. Finally, we end with discussion and conclusions sections.

2. Instrumentation and Meteorological Situation

a) Easton Site Instrumentation

The data for this analysis were collected as a part of the MASC + Radar project (MASCRAD; Notaros et al. 2016). The MASCRAD project involved the installation of a ground instrumentation site at the Easton Valley View Airport (Fig. 1). The South Platte River valley is located between the CSU-CHILL radar and the Easton site. The reduced terrain heights in the river valley combined with higher terrain elevations at Easton vs. CSU-CHILL (1432 m vs. 1460 m) allow clutter-free radar observations to be made at antenna elevations as low as 0.9° over Easton. At this elevation angle, the 0.33° wide CSU-CHILL X-band main beam illuminates a region located between 150 and 224 m above ground level over the Easton instrumentation site (13 km from the radar on an azimuth of 171°). To reduce the impact of horizontal wind on the precipitation observations, a 2/3-scale (8 m outer diameter) Double Fence Intercomparison Reference (DFIR) wind screen was constructed at Easton within which MASC and several other ground instruments were installed. The DFIR enabled substantial reduction in the horizontal winds (Notaros et al. 2016).

The basic MASC design includes three computer-controlled digital cameras located at 36° angular intervals around a horizontal plane. Hydrometeors falling towards the common viewing area of these three cameras pass through two infrared motion detection beams. The interruption of these beams triggers the cameras and their associated flash illumination systems. In the Colorado State University (CSU) MASC, the three horizontal plane cameras are Unibrain

980 digital camera. Each of these cameras generates 5 Mpixel files with a maximum resolution of 35 μm. The measurement area of the optical system is 18 cm^2. To improve 3D reconstructions of the imaged particles, two additional downward looking, lower-resolution cameras were added (Fig. 1 inset). While the processing of images collected by all five cameras can be done, only images from the three horizontal plane cameras that are the basis of the conventional MASC design were used in this analysis.

The MASC image pixels are recorded using 256 grayscale levels. This intensity data permits the extraction of various texture-based descriptors which are then used to automatically detect frozen cloud drops that accumulate on the outer surface of solid hydrometeors during riming, following the procedure introduced by Praz et al. (2017).

b) The CSU-CHILL Radar

The radar data presented here was collected with the CSU-CHILL operating in dual frequency mode (Junyent et al. 2015). In this configuration, a two frequency antenna feed allows dual polarization measurements to be made simultaneously at both 3 GHz (S-band) and 9 GHz (X-band). The same antenna reflector system is used at both frequencies, yielding a main (3 dB) beam width of 1.0° at S-band and 0.33° at X-band.

All of the radar data in this analysis was obtained from the CSU-CHILL X-band channel. This system uses a 25 KW peak power magnetron transmitter whose output is split, causing the antenna to simultaneously radiate both horizontally and vertically polarized waves. The reflectivity measurements obtained with the CSU-CHILL X-band system averaged within 1 dB of the values that were independently observed by a vertically-pointed, X-band continuous wave radar (Precipitation Occurrence Sensing System; Sheppard 1990) that was operating at Easton during the analyzed event. The CSU-CHILL Z_{DR} calibration was based on vertically pointed scans that were done at selected times when light precipitation was in progress at the radar site during the MASCRAD project. The Z_{DR} accuracy is estimated to be within ±0.12 dB.

c) Meteorological Situation

Salient features of the surface conditions during this event are summarized by the time history of the data collected at the Greeley-Weld County (KGXY) Automated Weather Observing System (AWOS) located ~11 km from the Easton site (Fig. 2). The color-coded sets of vertical lines in each panel of Fig. 2 mark the two time periods when different Z_{DR} regimes were noted in the immediate Easton area: During period 1 (26 November 2015, 18-20 UTC), Z_{DR} values averaged ~ +0.2 dB; in period 2 (27 November 2015, 02-0430 UTC), Z_{DR} was consistently more positive, averaging ~ +2.2 dB. Reflectivity levels were ~ 10 dBZ in period 1 and ~ 4 dBZ in period 2. The precipitation that occurred during this event was related to a shallow, anticyclonic upslope flow that developed the day after an initial surface cold front that passed the Greeley Airport near 1430 UTC on the morning of 25 November 2015. The accumulation rate of snow that occurs in this synoptic environment is generally light (Rasmussen et al. 1992). During period 1, surface winds were from the east-northeast at speeds of 4–5 ms^{-1} (Fig. 2a and b). These persistent synoptic scale upslope post-frontal surface winds resulted in the development of low clouds and periodic light snow in the Greeley area by time period 1. The cloud cover and low-level cold air advection kept surface temperatures at −6°C during most of the daylight hours (Fig. 2c). Around 21 UTC, wind directions became more northerly and speeds increased slightly to ~ 6 ms^{-1} (Fig. 2a and b). Two instances of gusting winds were reported in the 22–23 UTC period. The temperature and dew point traces show the arrival of colder, drier air associated with this wind shift (Fig. 2c). By the time of period 2, wind speeds decreased as a high pressure system moved into the area (Fig. 2b and d).

The overall evolution of the surface data suggests that during the earlier times, including period 1, the combination of upslope flow and subsequently enhanced convergence associated with the weak cold air surge that arrived around 21–22 UTC promoted the development of supercooled liquid water (Rasmussen et at, 1995). After ~ 00 UTC, upward air motions probably decreased as surface winds became light and colder, drier, high pressure conditions developed.

3. Data and Analyses

a) Radar Data

During the MASCRAD project, a prescribed sequence of scans that were focused on the Easton site were conducted by the CSU-CHILL radar. This sequence included a narrow (50° wide) Plan Position Indicator (PPI) volume with two elevation angles (0.9° and 1.5°). These were the lowest elevation angles that were free of ground clutter in the Easton area at S- and X-bands, respectively. Two sweep Range Height Indicator (RHI) scans were also done on azimuths that flanked the Easton site (171° and 172°; see Fig. 1). These scans were repeated at 3 minute intervals. Figure 3 shows representative X-band reflectivity and differential reflectivity (Z_{DR}) data collected during RHI scans in time periods 1 and 2 as identified in Fig. 2. In accordance with the generally weak synoptic scale forcing associated with the anticyclonic upslope environment, the echo depth was less than 2 km at both times (Fig. 3a and c). These echo top heights were also consistent with the base of a temperature inversion in the operational sounding data (not shown) from Denver, located ~70 km south of Easton. Reflectivities increased towards the ground at 1851 UTC during period 1, reaching 10–12 dBZ within 200 m of the surface at

Easton. In contrast, during period 2 at 0258 UTC, near-surface reflectivities generally remained below 6 dBZ. The Z_{DR} regimes were also quite different at these two times. At 1851 UTC, low-level Z_{DR} near Easton was very close to 0 dB; at 0258 UTC, the entire echo column within ±1 km of Easton contained Z_{DR} values of +3 dB or more (Fig. 3b and d).

The higher near-surface reflectivity and reduced Z_{DR} levels observed during period 1 indicate that the ice particles were larger and appearing more "spherical" as they descended to the ground. In contrast, during period 2, distinctly positive Z_{DR} values were observed in a low reflectivity environment. Hydrometeor classification schemes based on X-band radar data have associated these low reflectivity – positive Z_{DR} echo characteristics at subfreezing temperatures with the presence of relatively pristine planar ice crystals (Dolan and Rutledge 2009).

A more complete summary of the reflectivity and Z_{DR} contrasts observed between periods 1 and 2 is provided by the scatterplot shown in Figure 4. The data points were extracted from all of the 0.9° PPI sweeps done during these two time periods. Specifically, data from the range gates on this PPI scan surface that were located within a ±1 km range interval and a ±1° azimuth interval of Easton are plotted. During period 1, Z_{DR} remained near 0 dB despite Z_h variations of ~ 15 dB. In period 2, Z_{DR} was more positive, with the highest Z_{DR} tending to be associated with lowest reflectivities. Figure 4 also includes example MASC images from these two time periods. More riming is visibly evident on the crystal photographed during the higher reflectivity / low Z_{DR} conditions of period 1.

b) MASC Data

Image processing techniques to classify individual MASC snow particle images have recently been developed (Praz et al. 2017). In this effort, a regularized Multinomial Logistic

Regression (MLR) model was developed based on a training data set of approximately 3500 MASC images that had been manually classified with regard to particle type (among six predefined classes), presence of melting, and degree of riming. The classification was automated based on the distribution of 25 geometrical (e.g., particle maximum dimension, aspect ratio, shape complexity, and fractal dimension) and textural (e.g., mean brightness, local interpixel variability, and co-occurrence matrix) descriptors. For each individual image, the MLR model assigns a probability of belonging to each predefined class as well as a riming index, as illustrated in Fig. 5. These probabilities are then weighted over the three views of the same particle in order to assign a unique label for each hydrometeor.

The riming index is an indicator of the extent of riming on the surface of the particle. It is defined on a scale from zero to one with 0 indicating no cloud droplets visible on the particle surface and 1 indicating a graupel particle (i.e., complete obscuration of the initial particle by an extensive rime accumulation). The riming index assignment was based on a training data set in which the visually apparent degree of riming was put into one of five categories following Mosimann et al. (1994).

To relate the CHILL X-band Z_{DR} to the MASC-based riming index, all Z_{DR} range gate data within an area over and surrounding the MASCRAD site were extracted from the PPI sweeps, and a standard time-filtering procedure was applied (Lee 1980) in order to reduce the gate-to-gate fluctuations. Such filtering techniques had been shown to be in very good agreement with time-series of FIR (finite impulse response) range-filtered Z_{DR} (for example, see Fig. 2 of Thurai et al. 2012). The filtered Z_{DR} values were then time-interpolated to match the time of the MASC images. Finally, these filtered data were used to generate the riming index versus X-band Z_{DR} scatter plot shown in Fig. 6. Also shown in this plot are the means and standard deviations for the Z_{DR} and riming index data. Riming index values were higher during time period 1. The average riming index during period 1 (0.53) corresponds to continuous coating of cloud droplets on the frozen hydrometeor surfaces, while the 0.30 average value during period 2 indicates that the cloud droplet coverage was 50% or less.

The MASC images also provide information on particle aspect ratio (minor axis length / major axis length) and fall orientation. Both of these factors affect Z_{DR} (Bringi and Chandrasekar 2001). Orientation is usually described by the zenith angle (θ) and the azimuthal angle (ϕ) of the symmetry axis relative the local vertical Z-axis. For scattering analysis, the canting angle (β), which is the angle between the projection of the symmetry axis onto the polarization plane and the projection of the vertical direction (Z-axis) onto this same plane (Bringi and Chandrasekar 2001 Fig. 2.6a), is more relevant. At horizontal incidence, say along the X-axis and restricting the symmetry axis to be in the YZ plane, the canting angle is representative of θ. To make a correspondence with MASC definition of orientation angle, the vertical Z-axis is taken to be orthogonal to the horizontal plane (XY plane) where the cameras are located. For instance, the central camera can be considered to be located along the X-axis so the image from that camera will be in the YZ-plane. The orientation angle of the ellipse in this plane can be considered to be the canting angle. In the method of Praz et al. (2017), aspect ratio is based on the minor and major lengths of the ellipse that yields the least squares best fit to the particle's outer edge. Orientation angle is the rotation angle between major axis of this ellipse and the horizontal plane (between −90° and 90°). Henceforth, we will not distinguish between the orientation angle from the MASC and the canting angle relevant to the radar, and will frequently use "flutter" to characterize snow crystal fall mode. Finally, projected area is defined as the number of pixels included within a single particle's image.

Figure 7a shows the standard deviation of the orientation angle as a function of the minimum projected area for time periods 1 and 2, respectively. The X-axis values in this plot indicate the lowest projected area value for which the standard deviation of canting angle was calculated (for example, the standard deviation of canting angle associated with the 20 mm^2 X-axis value is based on the orientation angle data for all particles with a projected area of 20 mm^2 or larger). This method was used to separate the orientation angle fluctuations associated with the larger sized particles that provide greater contributions to the X-band radar returns. For projected areas larger than ~16 mm^2, the standard deviation of canting angle is larger in period 1; this period also had a relatively high riming index. The difference in the standard deviation of canting angle between these two periods approached a factor of 2 (~50° in period 1 vs. ~25° in period 2) for projected areas larger than ~28 mm^2. The DFIR wind screen, including the 2/3 scale design used at Easton, has been shown to achieve a snow collection efficiency of ~90% under the generally light (< 6 ms^{-1}) surface wind speeds (Rasmussen et al. 2012) that prevailed during this event. Based on this overall effectiveness of the DFIR wind screen design, we believe that these MASC-derived particle orientation angles were not significantly affected by instrument-induced turbulence. The increased standard deviation of orientation angle observed during period 1 is in qualitative agreement with the reduced Z_{DR} levels observed during this period (see Fig. 11 later in the text).

Additional characteristics of the orientation angle distributions are shown in Fig. 7b. This plot shows the mean and standard deviation of the canting angles associated with the same sequence of minimum projected area values that were used in Fig. 7a. For both periods 1 and 2, the magnitude of the mean canting angle generally was small (< 20°). (When averaging was done over all of the particle sizes, the magnitude of the mean canting angle was under 3° during both time periods). The wider distribution of canting angles, especially for projected areas larger than ~25 mm^2, during the riming conditions of time period 1 is evident.

The hydrometeor axis ratios derived from the MASC images recorded during analysis time period 1 and 2 are shown in Fig. 8. The axis ratio mean and standard deviation values are calculated and presented following the procedures that were used in Fig. 7b. While the axis ratios were consistently larger (more spherical) during period 1, the axis ratio differences between the two time periods cannot be considered to be statistically significant. In contrast to the standard deviation of canting angle distributions shown in Fig. 7b, significantly wider distributions of axis ratios were found during period 2. The reduced riming during period 2 allowed the more pristine ice crystals to retain their intrinsically low axis ratios. The presence of these low axis ratio particles broadened the ice particle axis ratio distribution.

The results of the MASC-based hydrometeor classification scheme were also examined for periods 1 and 2. As depicted in Fig. 5, the hydrometeor identification scheme presented in Praz et al. (2017) resolves six particle classifications. During the analyzed periods on 26–27 November 2015, no classifications in the combination of columns and plates category were made. A summary of the classification results, combined with the previously described riming index results, is presented in Fig. 9. The most frequently identified classifications in both time periods were planar crystals and aggregates. Graupel identifications, indicative of the most advanced stages of riming, were only observed during period 1 (Fig. 9a). This is in agreement with the generally higher riming index values that were generally found on all types of particles in period 1 relative to period 2.

Figure 9b shows the MASC image complexity value associated with each of the hydrometeor classes for time periods 1 and 2. The complexity number (similar to Garrett et al.

2012) is defined as the ratio of the perimeter length of the silhouette of the MASC particle image to the circumference of a circle of the same cross sectional area. Thus, a circular image results in a complexity value of 1.0; images with complicated perimeters, like branched ice crystals, etc. will have complexities greater than three. Complexity was uniformly higher during period 2 (low riming); in contrast, complexity was reduced in period 1 (more active riming). The higher riming indices recorded during period 1 are consistent with a more extensive rime coating that would produce smoother particle edges and fill in the ice structural irregularities (Moisseev et al. 2017).

4. Discussion

The event considered here involved a shallower, more simply organized echo system than the deep cyclonic type winter precipitation systems noted in Rasmussen et al (1992). Particle aggregation processes were not dominant in the sense that the MASC hydrometeor classifications consistently contained a significant fraction of individual ice crystals (Fig. 9). At the ~ −12°C echo top temperature level, growth of planar type ice crystals was favored (Bailey and Hallett 2009). The prevalence of such crystals is consistent with the tendency for more positive Z_{DR} values to be observed near echo top level (Williams et al. 2015).

During period 1, the slightly stronger upslope (easterly component) flow and pre-cold surge convergence at low levels were more favorable for the development of upward air motions and supercooled cloud droplets necessary for riming. The combination of increased riming index (0.5–0.6), lower complexity (< 2), and large standard deviation of canting angles of the larger particles (around 50°) during period 1 is consistent with rimed crystals and aggregates exhibiting complicated fall modes probably generated by spatial asymmetries in the growing rime deposit (Zikmunda and Vali 1972; Jayaweera and Mason 1965). This causes Z_{DR} to reduce dramatically (from the unrimed case) to near 0 dB. This interpretation differs from conventional arguments that increased riming of ice crystals during the early stages causes the aspect ratio to increase (i.e., more spherical) resulting in decrease of the Z_{DR} (Moisseev et al. 2017).

In contrast, during period 2, the riming index is much reduced (0.2–0.3), with large complexity (> 3), and much lower standard deviation of canting angles (20–30°) which are consistent with low flutter of the unrimed crystals leading to the conventionally observed higher Z_{DR} values in the range 2–3 dB (e.g., Matrosov et al. 2005; Williams et al. 2015). Figure 10 shows a schematic representation of the differences in the snow particle characteristics between periods 1 and 2 with the proviso that the mean aspect ratios inferred from MASC data are not significantly different between periods 1 and 2.

The premise that increased standard deviation of canting angles or flutter for plate-like crystals tends to decrease Z_{DR} is well-founded via scattering calculations using spheroid models (e.g., Bringi and Chandrasekar 2001; Melnikov and Straka 2013). An analytic equation derived by Jameson (1987) and, later, in a simpler manner by Bringi and Chandrasekar (2001) shows the essential features of this dependence which is more complex and involves the copolar correlation coefficient as well as linear depolarization ratio (LDR) (see Appendix). The assumptions are spheroid shapes with mean canting angle ≈ 0 and further for simplicity the copolar correlation coefficient ≈ 1 (the mean canting angle assumption is in agreement with MASC data in Fig. 7a whilst Melnikov and Straka 2013 show that the correlation coefficient is typically > 0.95 for plate-like crystals exhibiting flutter). Fig. 11 depicts the modeled behavior of Z_{DR} versus σ_β for two LDR values. The two points marked show [Z_{DR}, σ_β] for the two periods where Z_{DR} is based on averaged radar measurements whilst σ_β is based on MASC data in Fig. 7a for projected area > 30 mm^2 since the canting of the largest particles dominates the radar returns. The points representing periods 1 and 2 are on curves of constant but different LDR values, respectively, −32 and −20 dB. As mentioned in the Appendix, the sensitivity of the S-band cross-polar receiver precluded measurement of such low LDR signals. (The CSU-CHILL X-band system operates in simultaneous H and V transmission mode and thus cannot measure LDR). The higher LDR of −20 dB inferred during period 2 is consistent with [Z_{DR} = 2.5 dB; σ_β = 20°] and Eq. (A1). One reason for the high LDR during period 2 is likely related to the very large standard deviation in aspect ratios as shown in Fig. 8, especially for projected area > 20–30 mm^2. Equation (7.39) in Bringi and Chandrasekar (2001) shows that for a given σ_β and mean aspect ratio, the LDR can be enhanced by the variance of axis ratios which is not included in Eq. (A1). Such large values of LDR due to pristine dendrites exhibiting flutter have been measured, though at Ka-band, by Matrosov et al. (2005), who found values between −20 to −25 dB at low elevation angles. During period 1, the much lower LDR of −32 dB is consistent with [Z_{DR} = 0.5 dB; σ_β = 50°] and Eq. (A1). However, the standard deviation of axis ratios is much lower (see Fig. 8) especially for projected area > 30 mm^2 so that no enhancement of LDR due to this feature is expected.

5. Conclusions

The shallow-echo precipitation episode that affected the MASCRAD project area on 26–27 November 2015 provided a light snow regime where the aggregation process was restrained enough to preserve a detectable population of planar and columnar ice crystals based on the MASC particle classifications. Over the course of the event, the MASC image data showed significantly different degrees of particle riming between two time periods that contained contrasting Z_{DR} regimes. The MASC-based particle orientation and axis ratio measurements revealed the manner in which the riming affected hydrometeor physical properties that impact Z_{DR}. Specifically, the standard deviation of the hydrometeor canting angles was observed to be significantly larger during the time period when riming was more evident. These more random particle orientations contributed to the observed 1.5–2 dB reduction in Z_{DR}.

The relationship between Z_{DR} and hydrometeor riming is complicated (Moisseev et al. 2017; Vogel et al. 2015). Results differing from those obtained in this work should be expected in other meteorological and microphysical situations. It is anticipated that the high resolution particle photographs collected by the MASC, especially in conjunction with automated image processing techniques, along with other optical instruments that measure fall speeds and particle size distributions at high resolutions, will become increasingly useful. The measurements of these frozen hydrometeor physical characteristics are relevant to explain or model the interesting polarimetric radar signatures observed under different environmental conditions.

Acknowledgments

This work was supported by the US National Science Foundation under Grant AGS-1344862. Participation of Christophe Praz was funded through the Swiss National Foundation, under project number 200021_157210. We also thank the anonymous reviewers for providing input that significantly improved the paper.

APPENDIX

Z_{DR} and Standard Deviation of Canting Angle

To examine the relationship between Z_{DR} and standard deviation of canting angle, we make use of the equations provided in section 7.1.3 in Bringi and Chandrasekar (2001). In particular, equation (7.40a) can be used to derive an approximate variation between the two parameters. The equation can be rewritten as follows:

$$L = \frac{1}{4}(1 - \rho_4)\left\{1 - \frac{1}{\sqrt{z_{\mathrm{dr}}}}\right\}^2 \qquad \text{(A1)}$$

where

$$\rho_4 = e^{-8\sigma_\beta^2}$$

and L is the linear depolarization ratio (LDR), z_{dr} is Z_{DR} in linear units, and σ_β is the standard deviation of canting angles (the mean canting angle is assumed to be ≈ 0). Note that equation (A1) is applicable only when the copolar correlation coefficient approaches unity, and furthermore under the assumption of spheroidal shapes.

Equation (A1) can be rewritten as:

$$\frac{4L}{\left\{1 - \frac{1}{\sqrt{z_{\mathrm{dr}}}}\right\}^2} = 1 - \rho_4$$

which in turn can be recast as:

$$z_{\mathrm{dr}} = \left\{\frac{1}{1 - \sqrt{\frac{4L}{1 - \rho_4}}}\right\}^2 \qquad \text{(A2)}$$

In other words, the relationship between Z_{DR} and σ_β is dependent on L.

If we now input some example values for Z_{DR} (from CHILL X-band data) and for σ_β (determined from the MASC images) for the time periods, we obtain the following:

- For period 1, Z_{DR} = 0.5 dB; σ_β = 60°; calculated LDR ≈ −30 dB
- For period 2, Z_{DR} = 2.5 dB; σ_β = 20°; calculated LDR ≈ −20 dB

These are the two [Z_{DR}, σ_β] point pairs that are superimposed onto the two curves in Fig. 11. Note that the cross-polar S-band receiver sensitivity at the range to the Easton measurement site is not sufficient to measure LDR values as low as −20 dB under these weak copolar echo conditions.

References

Bailey, M. P. and J. Hallett, 2009: A comprehensive habit diagram for atmospheric ice crystals: Confirmation from the laboratory, AIRS II, and other field studies. *J. Atmos. Sci*., **66**, 2888–2899.

Botta, G., K. Aydin, J. Verlinde, A. E. Avramov, A. S. Ackerman, A. M. Fridlind, G. M. McFarquhar, and M. Wolde, 2011: Millimeter wave scattering from ice crystals and their aggregates: Comparing cloud model simulations with X- and Ka-band radar measurements. *J. Geophys. Res.*, **116**, D00T04, doi:10.1029/2011JD015909.

Bringi, V., and V. Chandrasekar, 2001: *Polarimetric Doppler Weather Radar: Principles and Applications.* Cambridge University Press, 636 pp.

Bringi, V.N., V. Chandrasekar, and R. Xiao, 1998: Raindrop axis ratios and size distributions in Florida rainshafts: An assessment of multiparameter radar algorithms. *IEEE Trans. Geosci. Remote Sens.*, **36**, 707–715.

Dolan, B. and S. A. Rutledge, A theory-based hydrometeor identification algorithm for X-band polarimetric radars. *J. Atmos. Oceanic. Tech.*, **26**, 2071–2088.

Garrett, T. J., C. Fallgatter, K. Shkurko, and D. Howlett, 2012: Fallspeed measurement and high-resolution multi-angle photography of hydrometeors in freefall. *Atmos. Meas. Tech. Discuss*., **5**, 4827−4850, doi:10.5194/amtd-5-4827-2012.

Garrett, T. J., S. E. Yuter, C. Fallgatter, K. Shkurko, S. R. Rhodes, and J. L. Endries, 2015: Orientations and aspect ratios of falling snow. *Geophys. Res. Lett.*, **42**, 4617–4622. doi: 10.1002/2015GL064040.

Giangrande, S. E., T. Toto, A. Bansemer, M. R. Kumjian, S. Mishra, and A.V. Ryzhkov, 2015: Insights into riming and aggregation processes as revealed by aircraft, radar, and disdrometer observations for a 27 April 2011 widespread precipitation event. *J. Geophys. Res. Atmos.*, **121**, 5846–5863.

Jameson, A.R., 1987: Relations Among Linear and Circular Polarization Parameters Measured in Canted Hydrometeors. *J. Atmos. Oceanic Technol.*, **4**, 634–646, https://doi.org/10.1175/1520-0426(1987)004<0634:RALACP>2.0.CO;2.

Jayaweera, K.O.L.F., and B. J. Mason, 1966: The falling motions of loaded cylinders and discs simulating snow crystals. *Q.J.R. Meteorol. Soc.*, **92**, 151–156. doi:10.1002/qj.49709239115.

Jensen, A. A., and J. Y. Harrington, 2015: Modeling Ice Cystal Aspect Ratio Evolution during Riming: A single-Particle Growth Model. *J. Atmos. Sci.*, **72**, 2569–2590.

Junyent, F., V. Chandrasekar, V. N. Bringi, S. A. Rutledge, P. C. Kennedy, D. Brunkow, J. George, and R. Bowie, 2015: Transformation of the CSU-CHILL Radar Facility to a Dual-Frequency, Dual-Polarization Doppler System. *Bull. Amer. Meteor. Soc.*, **96**, 975–996.

Kennedy, P. C. and S. A. Rutledge, 2011: S-band dual polarization radar observations of winter storms. *J. Appl. Meteor. and Climate*, **50**, 844–858.

Kuo, K., W.S. Olson, B.T. Johnson, M. Grecu, L. Tian, T.L. Clune, B.H. van Aartsen, A.J. Heymsfield, L. Liao, and R. Meneghini, 2016: The Microwave Radiative Properties of Falling Snow Derived from Nonspherical Ice Particle Models. Part I: An Extensive Database of Simulated Pristine Crystals and Aggregate Particles, and Their Scattering Properties. *J. Appl. Meteor. Climatol.*, **55**, 691–708, https://doi.org/10.1175/JAMC-D-15-0130.1.

Kumjian, M.R., A.V. Ryzhkov, H.D. Reeves, and T.J. Schuur, 2013: A Dual-Polarization Radar Signature of Hydrometeor Refreezing in Winter Storms. *J. Appl. Meteor. Climatol.*, **52**, 2549–2566, https://doi.org/10.1175/JAMC-D-12-0311.1.

Lee, J. S., 1980: Digital image enhancement and noise filtering by use of local statistics. *IEEE Trans. Pattern Anal. Mach. Intell.*, **2**, 165–168.

Lu, Y., Zhiyuan Jiang, Kultegin Aydin, Johannes Verlinde, Eugene E Clothiaux and Giovanni Botta, 2016, "A Polarimetric Scattering Database for Non-spherical Ice Particles at Microwave Wavelengths", *Atmos. Meas. Tech.*, **9**, 5119–5134.

Matrosov, S.Y., R.F. Reinking, R.A. Kropfli, B.E. Martner, and B.W. Bartram, 2001: On the Use of Radar Depolarization Ratios for Estimating Shapes of Ice Hydrometeors in Winter Clouds. *J. Appl. Meteor.*, **40**, 479–490, https://doi.org/10.1175/1520-0450(2001)040<0479:OTUORD> 2.0.CO;2.

Matrosov, S. Y., Reinking, R. F., Djalalova, I. V., 2005: Inferring Fall Attitudes of Pristine Dendritic Crystals from Polarimetric Radar Data, *J. Atmos. Sci.*, **62**, 241–250.

Melnikov, V. and J.M. Straka, 2013: Axis Ratios and Flutter Angles of Cloud Ice Particles: Retrievals from Radar Data. *J. Atmos. Oceanic Technol.*, **30**, 1691–1703, https://doi.org/10.1175/ JTECH-D-12-00212.1.

Moismann, L., E. Weingartner, and A. Waldvogel, 1994: An analysis of accreted drop sizes and mass on rimed snow crystals. *J. Atmos. Sci.*, **51**, 1548–1558.

Moisseev, D., A. von Lerber, and J. Tiira, 2017: Quantifying the effect of riming on snowfall using ground-based observations. *J. Geophys. Res. Atmos*., **122**, 4019–4037, doi:10.1002/ 2016JD026272.

Notaroš, B. M., V. N. Bringi, C. Kleinkort, P. Kennedy, G.-J. Huang, M. Thurai, A. J. Newman, W. Bang, and G. Lee, 2016: Accurate Characterization of Winter Precipitation Using Multi-Angle Snowflake Camera, Visual Hull, Advanced Scattering Methods and Polarimetric Radar.

Invited paper, Special Issue Advances in Clouds and Precipitation, *Atmosphere*, **7** (6), 81–111. doi: http://dx.doi.org/10.3390/atmos7060081.

Praz, C., Y. Roulet, and A. Berne, 2017: Solid hydrometeor classification and riming degree estimation from pictures collected with a Multi-Angle Snowflake Camera. *Atmos. Meas. Tech.*, **10**, 1335–1357. doi:10.5194/amt-10-1335-2017.

Rasmussen, R., B. Baker, J. Kochendorfer, T. Meyers, S. Landolt, A.P. Fischer, J. Black, J.M. Thériault, P. Kucera, D. Gochis, C. Smith, R. Nitu, M. Hall, K. Ikeda, and E. Gutmann, 2012: How Well Are We Measuring Snow: The NOAA/FAA/NCAR Winter Precipitation Test Bed. *Bull. Amer. Meteor. Soc.*, **93**, 811–829, https://doi.org/10.1175/BAMS-D-11-00052.1.

Rasmussen, R. M., B. Bernstein, M. Murakami, G. Stossmeister, and J. Reisner, 1995: The 1990 Valentine's Day Arctic Outbreak. Part I: mesoscale and Microscale Structure and Evolution of a Colorado Front Range Shallow Upslope Cloud. *J. Appl. Meteor*., **34**, 1481–1511.

Rasmussen, R. M., M. Politovich, J. Marwitz, W. Sand, J. McGinley, J. Smart, R. Pielke, S. Rutledge, D. Wesley, G. Stossmeister, B. Bernstein, K. Elmore, N. Powell, E. Westwater, B. Stankov, and D. Burrows, 1992: Winter Icing and Storms Project (WISP). *Bull. Amer. Meteor. Soc*., **73,** 951–974.

Ryzhkov, A., M. Pinsky, A. Pokrovsky, and A. Khain, 2011: Polarimetric Radar Observation Operator for a Cloud Model with Spectral Microphysics. *J. Appl. Meteor. Climatol.*, **50**, 873–894, https://doi.org/10.1175/2010JAMC2363.1.

Seliga, T.A. and V.N. Bringi, 1976: Potential use of radar differential reflectivity measurements at orthogonal polarizations for measuring precipitation. *J. Appl. Meteor*., **15**, 69–76.

Sheppard, B.E., 1990: Measurement of Raindrop Size Distributions Using a Small Doppler Radar. *J. Atmos. Oceanic Technol.*, **7**, 255–268, https://doi.org/10.1175/1520-0426(1990)007<0255:MORSDU>2.0.CO;2.

Smith, P.L., 1984: Equivalent Radar Reflectivity Factors for Snow and Ice Particles. *J. Climate Appl. Meteor.*, **23**, 1258–1260, https://doi.org/10.1175/1520-0450(1984)023<1258:ERRFFS>2.0.CO;2.

Thurai, M., V. N. Bringi, L. D. Carey, P. Gatlin, E. Schultz, and W. A. Petersen, 2012: Estimating the accuracy of polarimetric radar-based retrievals of drop size distribution parameters and rain rate: An application of error variance separation using radar-derived spatial correlations. *J. Hydrometeor.*, **13**, 1066–1079, doi:10.1175/JHM-D-11-070.1.

Vogel, J.M., F. Fabry, and I. Zawadzki, 2015: Attempts to observe polarimetric signatures of riming in stratiform precipitation. Extended abstract 6B.6. *American Meteorological Society's 37th Conference on Radar Meteorology*, 14-18 September, 2015, Norman, OK.

Williams, E.R., D.J. Smalley, M.F. Donovan, R.G. Hallowell, K.T. Hood, B.J. Bennett, R. Evaristo, A. Stepanek, T. Bals-Elsholz, J. Cobb, J. Ritzman, A. Korolev, and M. Wolde, 2015: Measurements of Differential Reflectivity in Snowstorms and Warm Season Stratiform Systems. *J. Appl. Meteor. Climatol.*, **54**, 573–595, https://doi.org/10.1175/JAMC-D-14-0020.1.

Wolde, M., and G. Vali, 2001a: Polarimetric signatures from ice crystals observed at 95 GHz in winter clouds. Part I: Dependence of crystal form. *J. Atmos. Sci.*, **58**, 828–841, doi: https://doi.org/10.1175/1520-0469(2001)058<0828:PSFICO>2.0.CO;2.

Zikmunda, J. and G. Vali: 1972: Fall patterns and fall velocities of rimed ice crystals. *J. Atmos. Sci.*, **29**, 1334–1347.

Figure Caption List

Figure 1: (a) MASCRAD instrumentation network and terrain height contours (m MSL) in the immediate CSU-CHILL radar – Easton area. The radar azimuths that flank the Easton site are shown in grey. (b) Overview of the ground instrument installation at Easton. (c) Close-up view of the MASC instrument as modified by CSU. The automated surface weather observations plotted in Fig. 2 were collected at the location marked KGXY AWOS, ~11 km from the MASC instrument at Easton.

Figure 2: Time history of Greeley Airport METAR data. Analysis time periods 1 and 2 are marked.

Figure 3: Example RHI data: Period 1 (a and b); period 2 (c and d). Red "E" marked along the range axis is the Easton site.

Figure 4: Extracted CHILL X-band Z and Z_{DR} data. Sample MASC images are shown for each of the two periods.

Figure 5: MASC automated data processing overview. The procedure is detailed in Section 3b. While the CSU MASC contains 5 cameras, the input to the automated processing system was restricted to images obtained from the three horizontal plane cameras.

Figure 6: Scatterplot of riming index derived from MASC particle image data vs. CSU-CHILL X-band Z_{DR} together with their corresponding means and standard deviations. The Z_{DR} data was extracted from the 0.9° elevation PPI scans azimuths that immediately flanked the MASC location at Easton. Within these radials, only range gates within ±1 km of the Easton range were considered. See text for the spatial and temporal filtering that was applied to the Z_{DR} gate data.

Figure 7: (a) Standard deviation of orientation angle vs. minimum projected area threshold for the MASC data collected during period 1 (purple) and period 2 (orange). Values based on less than 10 particle images are plotted in gray. (b) Means (dots) and standard deviations (bars) for the hydrometeor canting angles observed by the MASC during periods 1 (purple) and 2 (orange).

Figure 8: Means (dots) and standard deviations (bars) for the hydrometeor axis ratios observed during periods 1 and 2 vs. minimum projected area. Computations and plotting conventions as in Fig. 7b. Data from time period 1 is plotted in purple; time period 2 is plotted in orange.

Figure 9: (a) Riming index and MASC hydrometeor types. Abbreviated hydrometeor classifications are: Small particles (Small), Columnar Crystals (Col.Cry), Planar Crystals (Pl.Cry), Aggregates (Agg). Note: riming index results are not valid for the small particle category. (b) MASC image complexity number vs. MASC hydrometeor types. Numerical values, color coded by time period, along the abscissa indicate the number of individual MASC particle images that were included in each hydrometeor classification.

Figure 10: Schematic summary of the influence of riming on the polarimetric radar variables in the present case study. Z_{DR} is differential reflectivity, Ri is riming index, std is standard deviation of canting angle, AR is axis ratio, cplx is particle complexity.

Figure 11: Calculated Z_{DR} vs. standard deviation of canting angle for two LDR values (see the Appendix).

Figures

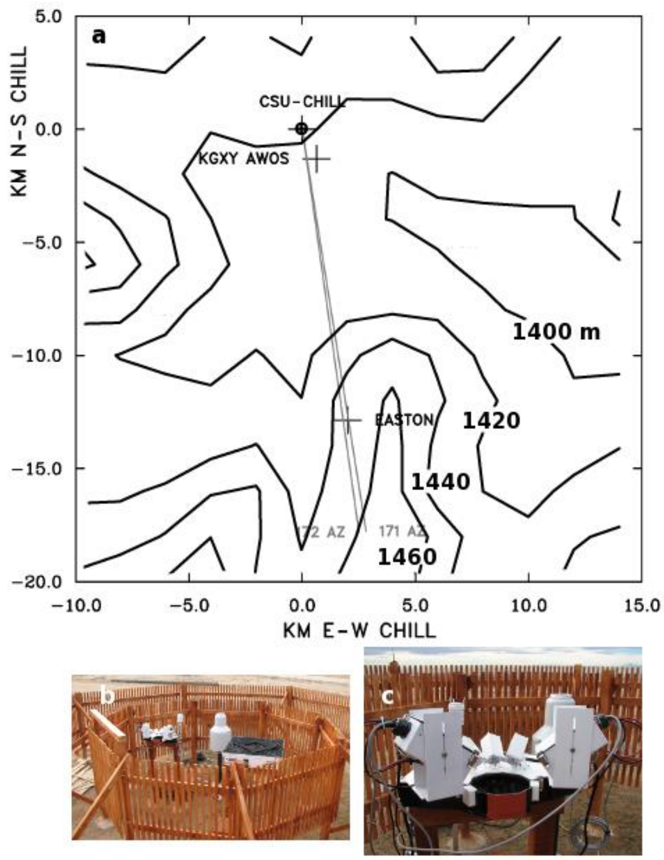

Figure 1: (a) MASCRAD instrumentation network and terrain height contours (m MSL) in the immediate CSU-CHILL radar – Easton area. The radar azimuths that flank the Easton site are shown in grey. (b) Overview of the ground instrument installation at Easton. (c) Close-up view of the MASC instrument as modified by CSU. The automated surface weather observations plotted in Fig. 2 were collected at the location marked KGXY AWOS, ~11 km from the MASC instrument at Easton.

.

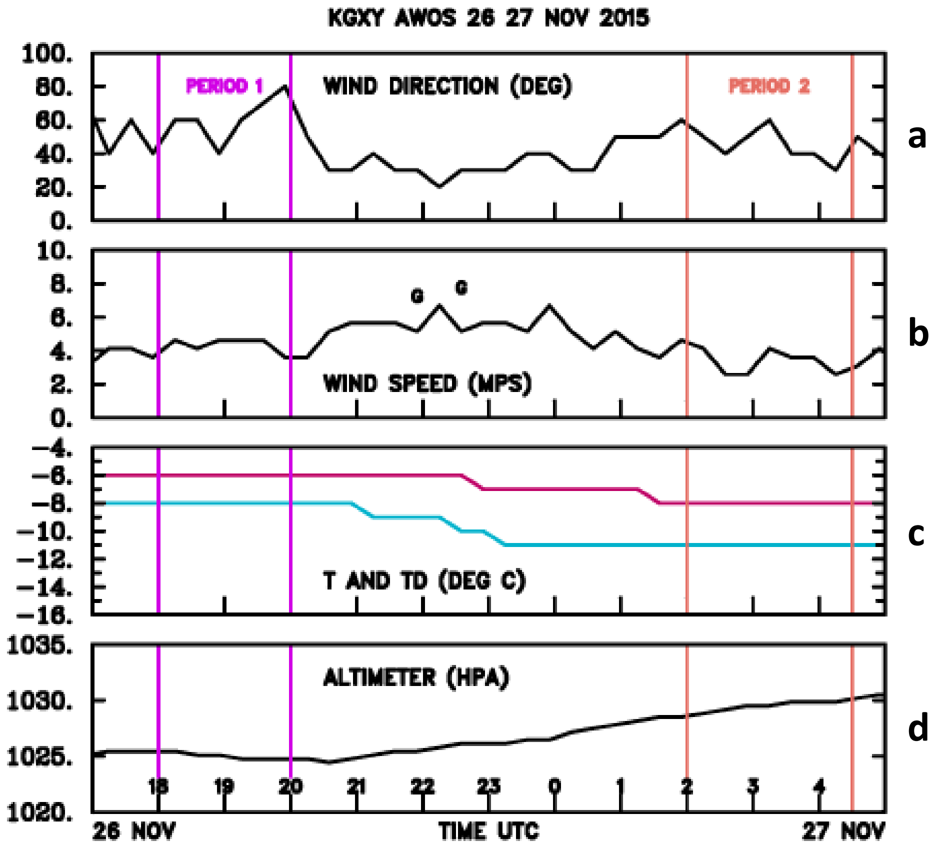

Figure 2: Time history of Greeley Airport METAR data. Analysis time periods 1 and 2 are marked.

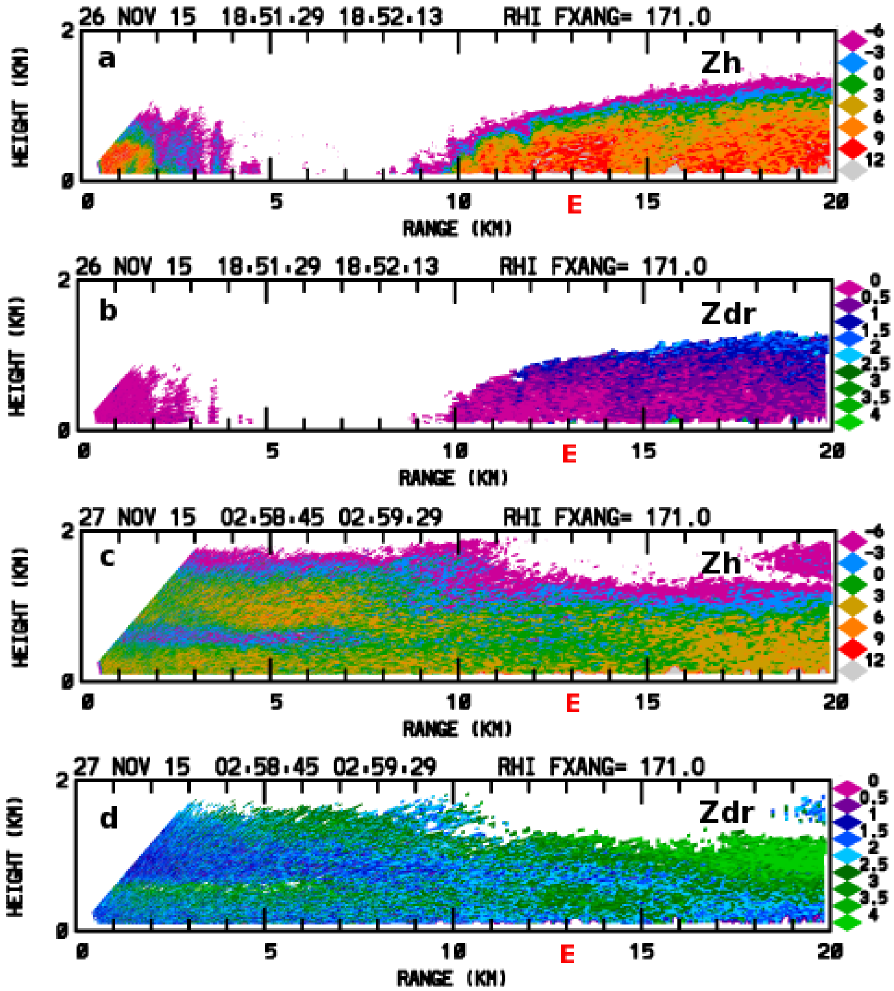

Figure 3: Example RHI data: Period 1 (a and b); period 2 (c and d). Red "E" marked along the range axis is the Easton site.

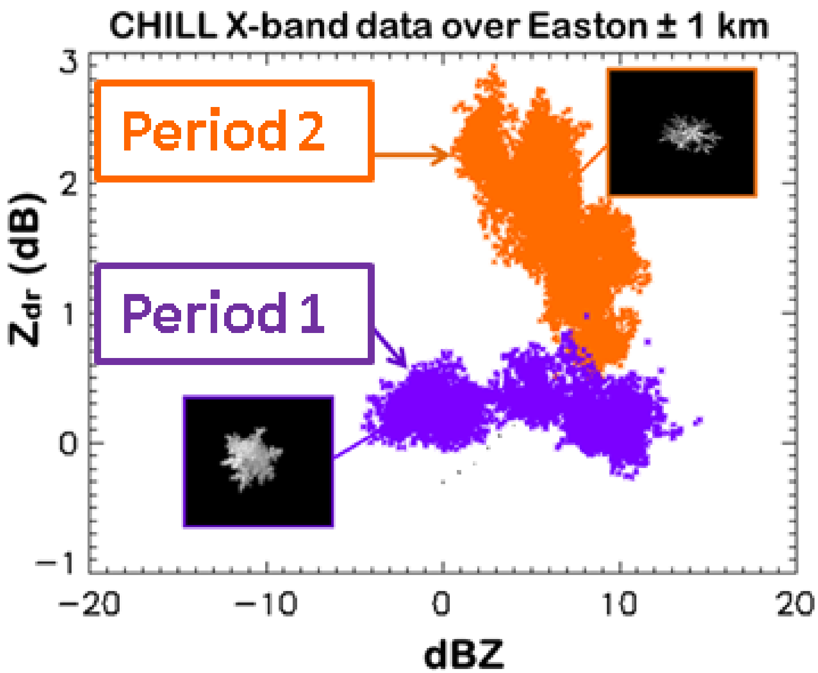

Figure 4: Extracted CHILL X-band Z and Z_{DR} data. Sample MASC images are shown for each of the two periods.

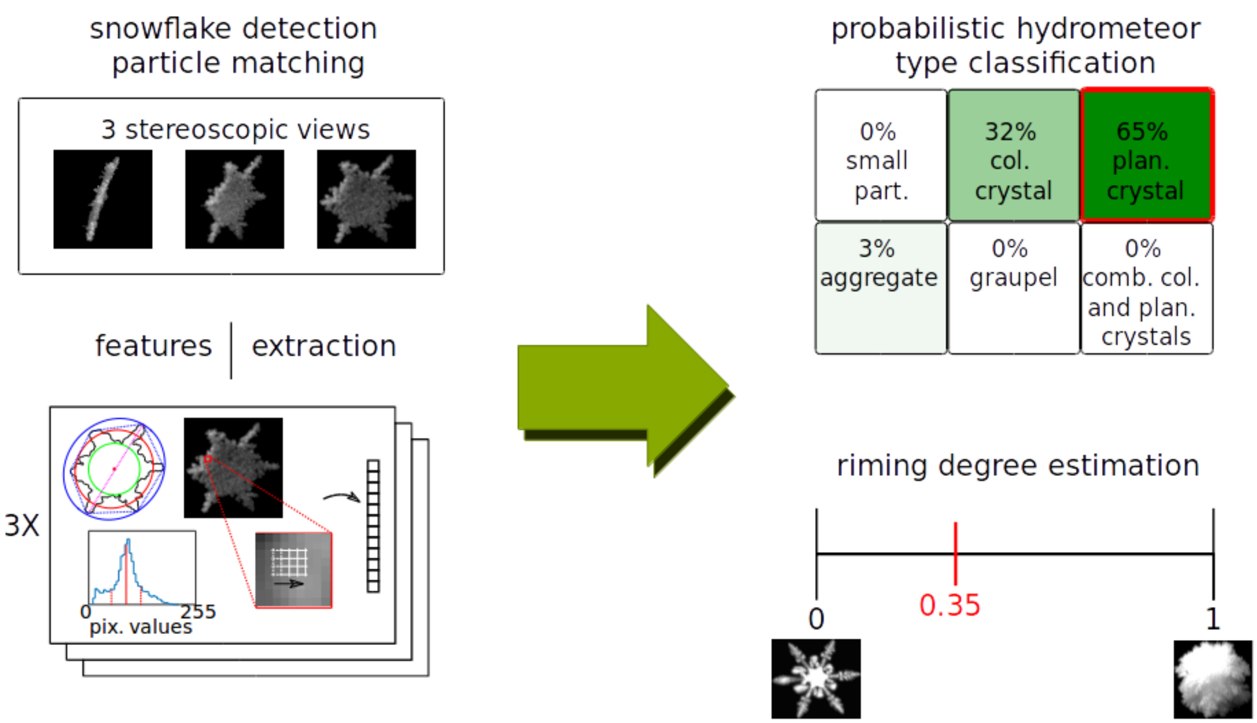

Figure 5: MASC automated data processing overview. The procedure is detailed in Section 3b. While the CSU MASC contains 5 cameras, the input to the automated processing system was restricted to images obtained from the three horizontal plane cameras.

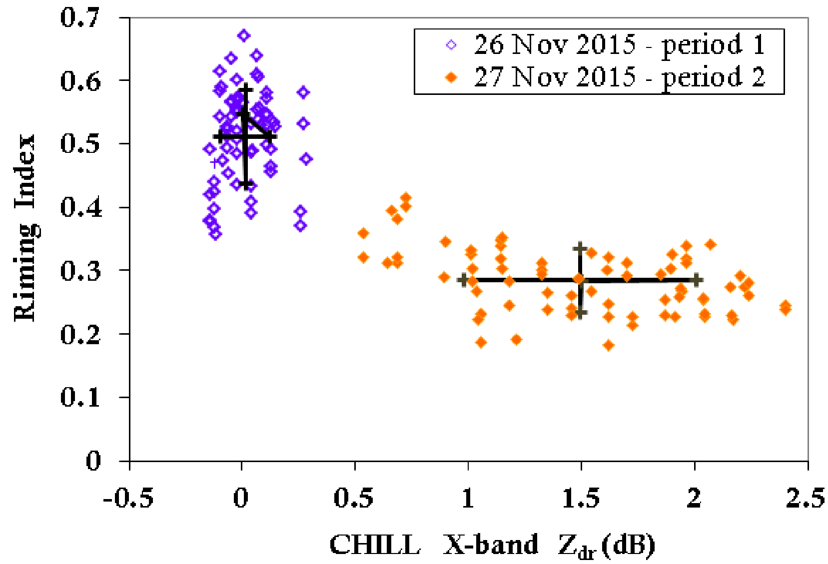

Figure 6: Scatterplot of riming index derived from MASC particle image data vs. CSU-CHILL X-band Z_{DR} together with their corresponding means and standard deviations. The Z_{DR} data was extracted from the 0.9° elevation PPI scans azimuths that immediately flanked the MASC location at Easton. Within these radials, only range gates within ±1 km of the Easton range were considered. See text for the spatial and temporal filtering that was applied to the Z_{DR} gate data.

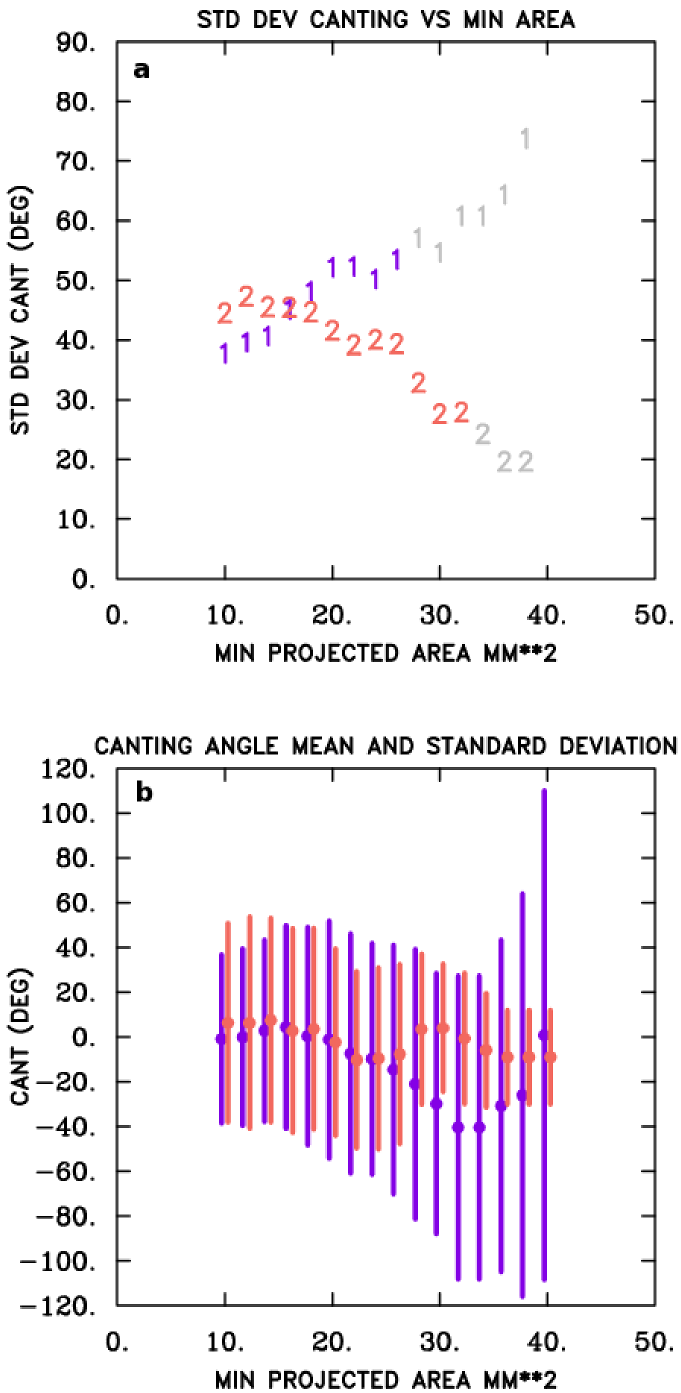

Figure 7: (a) Standard deviation of orientation angle vs. minimum projected area threshold for the MASC data collected during period 1 (purple) and period 2 (orange). Values based on less than 10 particle images are plotted in gray. (b) Means (dots) and standard deviations (bars) for the hydrometeor canting angles observed by the MASC during periods 1 (purple) and 2 (orange).

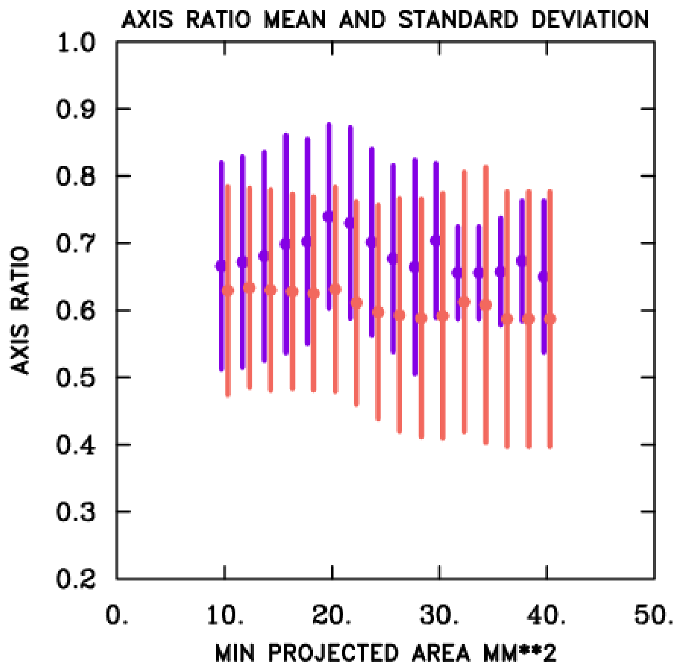

Figure 8: Means (dots) and standard deviations (bars) for the hydrometeor axis ratios observed during periods 1 and 2 vs. minimum projected area. Computations and plotting conventions as in Fig. 7b. Data from time period 1 is plotted in purple; time period 2 is plotted in orange.

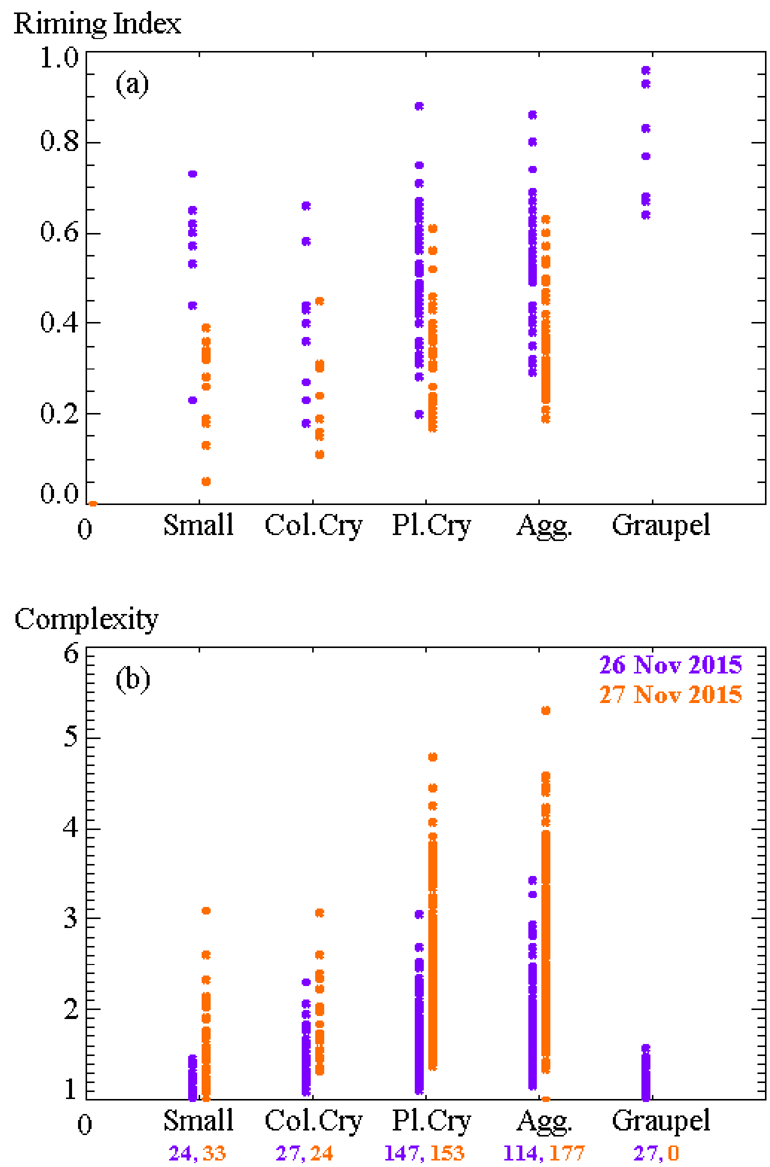

Figure 9: (a) Riming index and MASC hydrometeor types. Abbreviated hydrometeor classifications are: Small particles (Small), Columnar Crystals (Col.Cry), Planar Crystals (Pl.Cry), Aggregates (Agg). Note: riming index results are not valid for the small particle category. (b) MASC image complexity number vs. MASC hydrometeor types. Numerical values, color coded by time period, along the abscissa indicate the number of individual MASC particle images that were included in each hydrometeor classification.

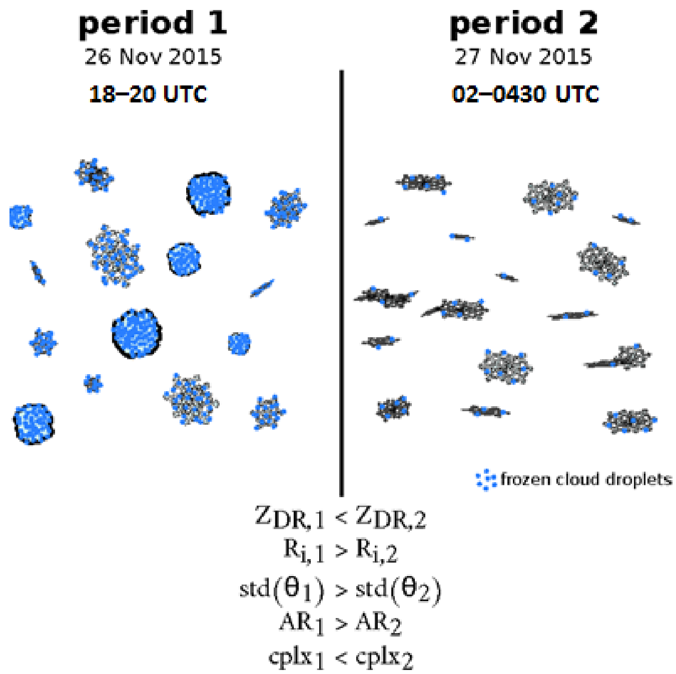

Figure 10: Schematic summary of the influence of riming on the polarimetric radar variables in the present case study. Z_{DR} is differential reflectivity, Ri is riming index, std is standard deviation of canting angle, AR is axis ratio, cplx is particle complexity.

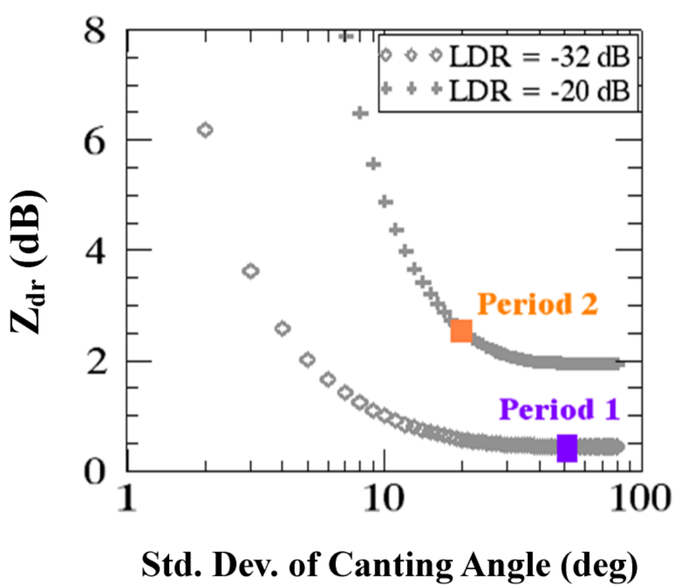

Figure 11: Calculated Z_{DR} vs. standard deviation of canting angle for two LDR values (see the Appendix).